Karim, M. R., Rahman, B. M., Azabi, Y. O., Agrawal, A. & Agrawal, G. P. (2015). Ultra-broadband mid-infrared supercontinuum generation through dispersion engineering of chalcogenide microstructured fibers. Journal of the Optical Society of America B, 32(11), pp. 2343-2351. doi: 10.1364/JOSAB.32.002343

Ultra-broadband mid-infrared supercontinuum generation through dispersion engineering of chalcogenide microstructured fibers

M. R. KARIM[1,*], B. M. A. RAHMAN[1], Y. O. AZABI[1], A. AGRAWAL[1], AND GOVIND P. AGRAWAL[2]

[1] School of Mathematics, Computer Science and Engineering, City University London, Northampton Square, London, EC1V 0HB, UK
[2] The Institute of Optics, University of Rochester, Rochester, New York, 14627, USA
[*] Corresponding author: mohammad.karim.2@city.ac.uk

We demonstrate numerically that the use of dispersion-engineered microstructured fibers made with chalcogenide glasses allows one to generate ultra-broadband supercontinuum spectra in the mid-infrared region by launching optical pulses at a suitable wavelength. As a specific example, numerical simulations show that such a 1-cm-long fiber, made with $Ge_{11.5}As_{24}Se_{64.5}$ glass and pumped at a wavelength of 3.1 μm using short pulses with a relatively modest peak power of 3 kW, can produce a spectrum extending from 1.3 μm to beyond 11 μm (more than 3 octaves). We consider three fiber structures with microstructured air holes in their cladding and find their optimum designs through dispersion engineering. Among these, equiangular-spiral microstructured fiber is found to be the most promising candidate for generating ultrawide supercontinuum in the mid-infrared region.

OCIS codes: *(000.4430) Numerical approximation and analysis; (190.0190) Nonlinear optics; (060.4005) Microstructured fibers; (320.6629) Supercontinuum generation.*

1. INTRODUCTION

Supercontinuum (SC) sources operating in the mid-infrared (MIR) wavelength region have attracted much attention because of their potential applications in molecular spectroscopy [1], frequency metrology [2], optical coherence tomography [3], biomedical imaging [4], and optical sensing. Most of the earlier theoretical and experimental investigations on SC generation focused on fiber-based geometries, particularly on photonic crystal fibers (PCFs) made with silica glass, since dispersion of PCFs could be easily engineered owing to a strong modal confinement associated with the presence of air holes inside PCF's cladding [5–10]. Although strong mode confinement can be achieved in silica PCF, the relatively weak nonlinearity of silica necessitates high peak powers for SC generation. Moreover, as silica suffers from severe absorption at wavelengths beyond 2.2 μm, it is not possible to extend the generated SC far into the MIR regime [11].

Recently attention has focused on chalcogenide (ChG) glasses because these glasses exhibit high optical nonlinearities (several hundred times that of silica), are transparent in the MIR region, and can be easily drawn into a fiber form [12]. Clearly, ChG fibers can be used to develop a SC source providing wavelengths beyond 5 μm, where the propagation losses of silica, ZBLAN, and tellurite fibers become intolerably large. ChG glasses can provide MIR transparency up to 14 μm when selenide-based materials are employed [13]. Since GeAsSe glasses have excellent film-forming properties and possess a relatively high third-order nonlinearity, there has been growing interest in using them for designing planar waveguides for broadband MIR SC generation [14]. In one approach, ultrashort pump pulses are launched into a dispersion-engineered planar waveguide. However, this approach suffers from cladding absorption and cut-off of the fundamental mode when an asymmetric structure is employed. A fiber-based device remain attractive because of its ruggedness, excellent beam quality, and relative ease of manufacturing [15]. Microstructured fibers are attractive due to their inherent advantages such as a controllable mode area and desirable dispersion properties achieved through tailoring their structural parameters. PCFs are particularly attractive as they offer significant enhancement of the nonlinear effects owing to a strong mode confinement and easier dispersion management resulting from the use of a cladding containing air holes [16].

Several experimental and theoretical investigations on MIR SC generation have already been reported using both ChG planar wavegiudes [17–21] and ChG fibers [22–27]. Gai *et al.* [17] used a 6.6-cm-long rib waveguide made of As_2S_3 glass to generate a SC spanning from 2.9 to 4.2 μm, when pumped at a wavelength of 3.26 μm with 7.5 ps duration pulses with 2-kW peak power. Yu *et al.* [18] found theoretically that, by using a dispersion-engineered, $Ge_{11.5}As_{24}Se_{64.5}$ rib waveguide, the SC could be extended beyond 10 μm pumped using 250 fs duration pulses at a wavelength of 4 μm or longer. Yu *et al.* [19] later

produced a broadband SC extending from 1.8 to 7.5 μm in a 1-cm-long rib waveguide, pumped at 4 μm using 320 fs pulses with 3.26 kW peak power. Recently Karim *et al.* [20] found theoretically that a broadband SC extending from 1.9 to 11 μm could be generated using a 1-cm-long, dispersion-engineered, $Ge_{11.5}As_{24}Se_{64.5}$ channel waveguide pumped using pulses with 3 kW peak power. Liang *et al.* [21] experimentally investigated the MIR SC spanning up to 5 μm in 8-mm-thick bulk dielectric filament made using ZnS with normal GVD regime pumped at 2.1 μm. In the case of optical fibers, Salem *et al.* [22] numerically demonstrated MIR SC extending in the range 3.14-6.33 μm by using 8-mm-long tapered As_2S_3 PCF with input pulse energy of 100 pJ pumped at 4.7 μm. Kubat *et al.* [23] reported a approach for generating MIR SC spanning in the range 0.9-9 μm by using concatenated 10-m-long fluoride and 10-cm-long chalcogenide fibers using a Tm fiber laser with a duration of 3.5-ps at a wavelength of 2 μm. Hudson *et al.* [24] used a As_2S_3 fiber to generate a SC spanning from 1.6 to 5.9 μm by pumping it at 3.1 μm using pulses with 520 kW peak power. Petersen *et al.* [25] produced a SC extending from 1.4 to 13.3 μm using a 8.5-cm-long As_2S_3 fiber pumped with 100-fs pulses at a wavelength of 6.3 μm. Møller *et al.* [26] generated a SC extending from 1.7 to 7.5 μm using a 18-cm-long, suspended core, $As_{38}S_{62}$ fiber pumped at a wavelength of 4.4 μm using 320-fs pulses with 5.2 kW peak power. Yu *et al.* [27] recently reported that a SC extending from 1.8 to 10 μm could be generated in a 11-cm-long, GeAsSe-based fiber using 320-fs pump pulses at a wavelength of 4 μm with a moderate peak power of 3 kW.

The main problem with all planar or fiber-based ChG waveguides reported so far is the cladding absorption at the long-wavelength edge. For example, Yu *et al.* produced MIR SC using either an asymmetrical ChG rib-waveguide (wavelength range 1.8-7.5 μm) [19] or a ChG step-index fiber (wavelength range 1.8-10 μm) [27]. In both cases, a ChG sulphide-based material was used for the cladding, which has a transmission limit of 8.5 μm, resulting in considerable cladding losses at wavelengths beyond 8.5 μm. Although a ChG selenide-based material has transparency up to 14 μm, its use leads to cut-off of the fundamental mode at long wavelengths owing to asymmetrical nature of the waveguide. Moreover, high absorption in the fluoro-polymer coating on top of the planar waveguide make it difficult to extend the SC beyond 10 μm. Recently we proposed a channel waveguide with air on top and either $Ge_{11.5}As_{24}S_{64.5}$ or MgF_2 glass as the lower cladding material that enables us to extend the SC in the MIR region up to 11 μm [20]. In this work, absorption of MgF_2 glass beyond 9 μm limited the long-wavelength extension of the generated SC.

In this paper, we show numerically that a 1-cm-long, dispersion-tailored, $Ge_{11.5}As_{24}Se_{64.5}$ fiber with a PCF structure containing air holes in its cladding, can be used to generate a ultrawide SC in the MIR regime. Three different designs are proposed in this study: (1) a triangular-core fiber, (2) a conventional hexagonal PCF, and (3) an equiangular spiral PCF (ES-PCF). Among these, the ES-PCF was found to be most promising for generating ultrawide SC in the MIR regime. Currently a number of researchers are focusing on MIR SC generation using a Tm doped fiber laser which emits pump pulses at a wavelength of around 2 μm. However, it is not possible to achieve long wavelength extension of SC far into the MIR region by using such pump sources. Several research groups have shown experimentally that the extension of SC in the long wavelength region depends on the availability of pump pulses at a suitable wavelength. In particular, the pump wavelength needs to be near 3-4 μm or longer. To tailor the dispersion around this pump wavelength, the effective mode area of the waveguide is often increased which, in turn, deceases the nonlinear parameter of the waveguide. Since the Kerr coefficient of a ChG waveguide also decreases with the increasing pump wavelength, high pump powers are required to extend SC in the long-wavelength region, which can cause damage to ChG PCFs if relatively wide pump pulses with high peak powers are employed [18]. For our numerical simulations, we employ pump pulses of 85-fs duration (FWHM) at a wavelength of 3.1 μm with a repetition rate of 160 kHz [31]. The peak power of pump pulses is varied in the range of 0.2 to 3 kW. We show that a SC covering the wavelength range from 1.3 to 11 μm (>3 octaves at the −30 dB level from the peak) can be generated with our proposed ChG ES-PCF at a relatively modest peak power of 3 kW.

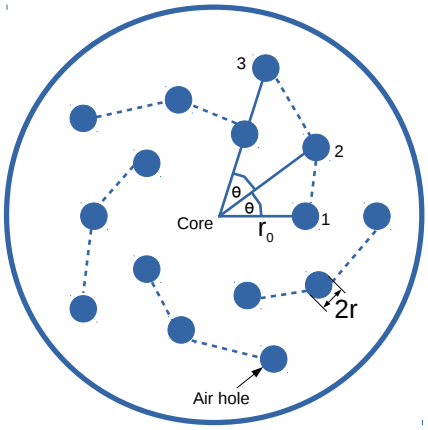

Fig. 1. ChG equiangular spiral PCF geometry used for dispersion optimization.

2. DESIGN PRINCIPLE

The wavelength-dependent linear refractive index n of $Ge_{11.5}As_{24}Se_{64.5}$ chalcogenide glass over the entire wavelength range used in the numerical simulations is given by the Sellmeier equation [14],

$$n(\lambda) = \sqrt{1 + \frac{5.78525\lambda^2}{\lambda^2 - 0.28795^2} + \frac{0.39705\lambda^2}{\lambda^2 - 30.39338^2}}, \quad \textbf{(1)}$$

where λ is the wavelength in micrometers.

The generation of a supercontinuum covering a wide spectral range at the output of an optical waveguide involves a complex interplay among a multitude of linear and nonlinear phenomena occurring simultaneously during the propagation of an optical pulse along the waveguide length. Group velocity dispersion (GVD) of the waveguide plays an important role in producing such a supercontinuum. More specifically, a relatively small anomalous GVD is required over a wide wavelength range for realizing large frequency shifts of the Raman soliton forming inside the microstructured fibers. To realize a microstructured fiber with its zero-dispersion wavelength (ZDW) close to the pump wavelength, relatively large waveguide dispersion is required to offset the material dispersion. For accurate numerical simulations, it is essential that dispersive properties of the fiber are

calculated as precisely as possible. The accuracy of dispersion parameters depend on how accurately calculates the mode propagation, $\beta(\omega)$ for the fundamental mode through modal solution of a waveguide. Therefore, accuracy of any design critically depends on the accuracy of modal solutions of a waveguide. For our proposed microstructured fibers, we represent the waveguide structures with 360,000 first order triangular elements to obtain higher accuracy modal solutions. We use a finite-element method (FEM) based, full-vectorial mode solver [30] to obtain the propagation constant of the fundamental mode over a wide range of wavelengths. To calculate the effective mode index, which is used for calculating GVD and various higher-order dispersion coefficients, we utilize the mode propagation constant obtained by our FEM solver. The effective mode index of the fundamental mode is calculated up to fifteenth decimal place so as to accurately determine the GVD and higher-order dispersion coefficients. To examine the accuracy of the finite-element modal solutions for our ChG PCFs, we tested the FEM results by Aitken's extrapolation [13] through convergence between the raw FEM results and extrapolated values as the number of mesh elements increased.

The ES-PCF used in our study is a modified version of that reported in Ref. [32–34]. Figure 1 shows the five-arm air-hole arrangement for our ES-PCF. Its spiral pitch (Λ_s) in polar coordinates is given by

$$\Lambda_s = r_0\, e^{\theta\, \cot\alpha}, \tag{2}$$

where r_0 is the initial spiral radius (see Fig. 1), θ is the angular increment between two successive air-holes in the same arm, and α is the angle between the radial line (Λ_s) and the tangent drawn on the equiangular spiral curve.

The FEM is a well established numerical method for the solution of a wide range of guided-wave problems. It can be easily applied to optical waveguides with any refractive index distribution and to those with anisotropic or nonlinear materials. The FEM is based upon dividing the waveguide region into a large number of non-overlapping patchwork of polygons, usually triangular elements. The field over each element is then expressed in terms of polynomials weighted by the fields over each element. By differentiating the functional with respect to each nodal value, the problem is reduced to a standard eigenvalue matrix equation, which is solved to obtain the propagation constants $\beta(\omega)$ and field profiles of various modes. In the full-vectorial formulation one needs to minimize the full **H**-field energy functional using [30],

$$\omega^2 = \frac{\iint \left[(\nabla\times\mathbf{H})^*.\hat{\varepsilon}^{-1}(\nabla\times\mathbf{H}) + p(\nabla.\mathbf{H})^*(\nabla.\mathbf{H})\right] dxdy}{\iint \mathbf{H}^*.\hat{\mu}\mathbf{H}\, dxdy}, \tag{3}$$

where **H** is the vectorial magnetic field, * denotes a complex conjugate and transpose, ω is the angular frequency, p is a weighting factor for the penalty term to eliminate spurious modes, and $\hat{\varepsilon}$ and $\hat{\mu}$ are the permittivity and permeability tensors, respectively.

To study the formation of SC inside the waveguide, we model the pulse evolution inside the microstructured fibers with a generalized nonlinear Schrödinger equation (GNLSE) [13]:

$$\frac{\partial}{\partial z}A(z,T) = -\frac{\alpha}{2}A + \sum_{m\geq 2}^{10}\frac{i^{m+1}}{m!}\beta_m\frac{\partial^m A}{\partial T^m} + i\left(\gamma + i\frac{\alpha_2}{2A_{\text{eff}}}\right)\left(1+\frac{i}{\omega_0}\frac{\partial}{\partial T}\right) \times \left(A(z,T)\int_{-\infty}^{\infty} R(T)\mid A(z,T-T')\mid^2 dT'\right), \tag{4}$$

where $A(z,T)$ is the slowly varying envelope of the pump pulse in a retarded time frame $T = t - \beta_1 z$ moving at the group velocity $1/\beta_1$, β_m ($m \geq 2$) is the mth order dispersion parameter, α accounts for linear propagation losses, and ω_0 is the pump frequency. The nonlinear coefficient is defined as $\gamma = n_2\omega_0/(cA_{\text{eff}})$, where n_2 is the nonlinear refractive index, c is the speed of light in vacuum, A_{eff} is the effective area of the mode at the pump frequency, and $\alpha_2 = 9.3\times10^{-14}$ m/W is the two-photon absorption coefficient [20]. The material response function $R(t)$ includes both the instantaneous Kerr response, $\delta(t)$, and the delayed Raman response, $h_R(t)$, expressed as

$$R(t) = (1-f_R)\delta(t) + f_R h_R(t), \tag{5}$$

$$h_R(t) = \frac{\tau_1^2+\tau_2^2}{\tau_1\tau_2^2}\exp\left(-\frac{t}{\tau_2}\right)\sin\left(\frac{t}{\tau_1}\right), \tag{6}$$

where $f_R = 0.031$, $\tau_1 = 15.5$ fs, and $\tau_2 = 230.5$ fs for ChG material [13].

One may ask whether GNLSE can be used to model spectra whose bandwidth becomes comparable to the carrier frequency ω_0 of the pump pulse used to produce the supercontinuum. Blow and Wood suggested in 1989 that GNLSE can be used as long as the total bandwidth remains below $\omega_0/3$ [29]. In reality, the prediction of GNLSE appears to match the experimental data on supercontinuum generation reasonably well even when this condition is violated. The reason, in our opinion, is related to the fact that the supercontinuum output in our numerical simulations consists of multiple subpulses with overlapping spectra such that the spectrum of each subpulse satisfies the preceding criterion.

3. DISPERSION ENGINEERING THROUGH MICROSTRCTURING

For studying SC generation, we numerically solve Eq. (4) with the split-step Fourier method including dispersion terms up to tenth order. As discussed earlier, a broadband MIR SC is obtained by using a pump wavelength close to the ZDW of the waveguide. Several techniques have been used to shift the ZDW of $Ge_{11.5}As_{24}Se_{64.5}$ ChG material (located near 7 μm) toward a shorter wavelength near 3 μm [1, 11, 28]. Here, we have designed and optimized three different $Ge_{11.5}As_{24}Se_{64.5}$ PCFs by micro-structuring air holes in the cladding. Such microstructuring allows us to fine tune/adjust fiber's ZDW over a much wider wavelength range compared to that of planar waveguides and conventional fibers.

To shift the ZDW of our ChG fiber near 3.1 μm with a relatively small value of anomalous dispersion at the pump wavelength, we consider several PCF designs. In one design the PCF has three large air holes forming a triangular core in the center. Figure 2(a) shows the numerically calculated GVD curves when each side of the triangle is $a = 6$ or 7 μm long. The resulting field profile for the fundamental mode at the pump wavelength is shown as an inset in the 6 μm case. The second configuration we study corresponds to the case of a conventional hexagonal PCF. In this case, air holes follow a hexagonal pattern around a central core. Both the diameter (d) and pitch (Λ) of the air holes can be varied to engineer PCF's dispersive properties. Figure 2(b) shows the GVD curves when the ratio d/Λ is 0.6 or 0.8 while Λ is kept constant at a value of 3 μm. It is apparent from these curves that the second configuration is better since such a PCF exhibits two ZDWs in the MIR region that are spaced far apart. As a result, it is possible to realize relatively small

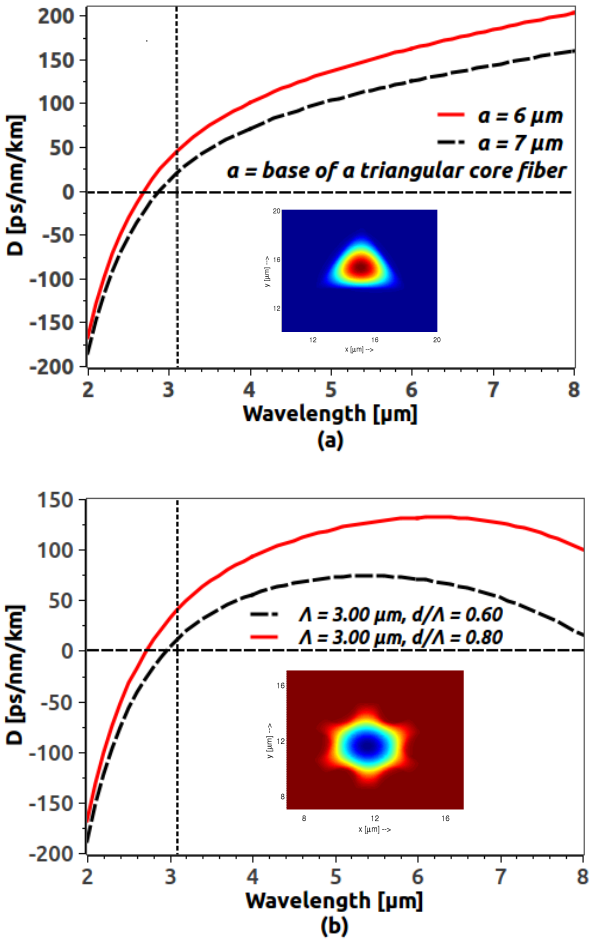

Fig. 2. Dispersion curves for two ChG microstuctured fibers designs. (a) Triangular core fiber with side lengths $a = 6$ or 7 μm; (b) Hexagonal PCF for different d/Λ values with Λ constant. Vertical dotted line indicates pump wavelength and the inset shows the spatial profile of the fundamental mode at a wavelength of 3.1 μm.

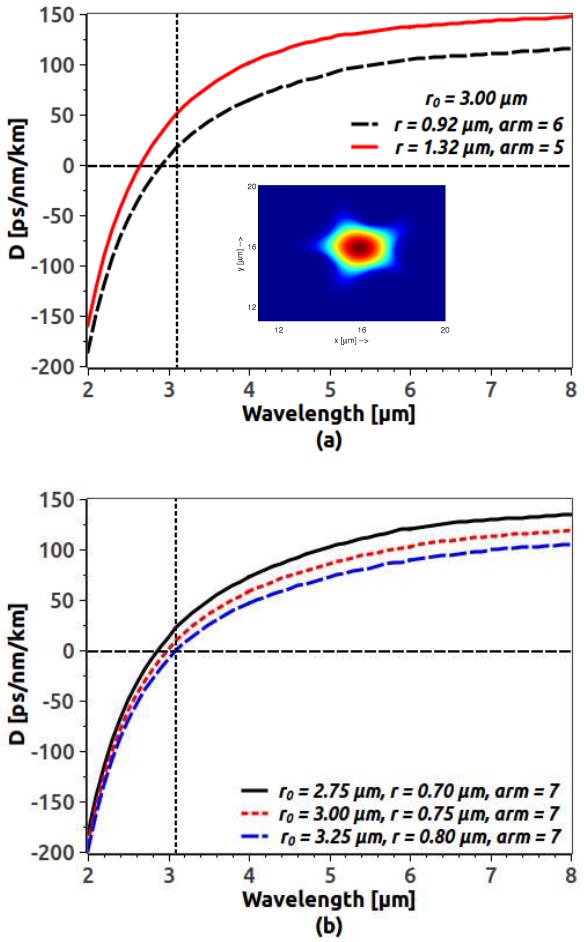

Fig. 3. Dispersion curves for the ChG ES-PCF design shown in Fig. 1 when (a) air-hole radius (r) and number of spiral arm are varied while keeping spiral radius (r_0) constant; (b) r_0 and r are varied with keeping number of spiral arm constant. Vertical dotted line indicates pump wavelength and the inset shows the spatial profile of the fundamental mode at a wavelength of 3.1 μm.

anomalous dispersion over a wide wavelength range extending from 2.7 μm to beyond 8 μm. In addition, the spatial profile of the fundamental mode, shown as an inset of Fig. 2(b), exhibits excellent field confinement to the central core region, enabling enhanced nonlinear interaction.

The third fiber design we consider is the ES-PCF shown in Fig. 1. We varied design parameters over a wide range and optimized them to obtain the two sets of GVD curves shown in Figs. 3(a) and 3(b). In both cases, the ES-PCF has 3 rings of air holes but other parameters are varied. In Fig. 3(a), the solid red curve corresponds to a fiber with 5 spiral arms, a spiral radius r_0 = 3 μm, a spiral angle $\theta = 36^\circ$, and a hole radius r = 1.32 μm; the dashed black curve is obtained for 6 spiral arms, $\theta = 30^\circ$, and r = 0.92 μm, while keeping other parameters the same. In the case of Fig. 3(b), we change the parameters r_0 and r while keeping the number of arms fixed at 7. The important point to note is that the ES-PCF design allows us to obtain much flatter dispersion over a wider wavelength range compared to traditional PCF designs shown in Fig. 2. The choice of four structural parameters (r_0, r, θ, and number of spiral arms) makes it easier to tailor an ES-PCF such that its ZDW is near the 3.1 μm pump wavelength with a GVD that is is anomalous and flatter than conventional PCFs over a wide wavelength range. Physically, air holes of each ring in ES-PCF revolve with respect to the previous ring, which effectively stops the field spreading into the regions between air holes and confines it tightly in the core region.

One has to be careful while designing an ES-PCF. Since the spiral pitch Λ_s varies with the spiral radius r_0, angular progression θ, and the tangent angle, α, there is a possibility that two nearby air holes may merge together if the structural parameters of ES-PCF are not chosen correctly. To avoid this, we adopted a hole-merging check during numerical simulations. For the GVD curves shown in Fig. 3(a), we ensured that the minimum separation between air holes was 265 nm. In fact, average air-hole separation was 4.66 μm for the red curve. For the black dispersion curve in Fig. 3(a), the minimum separation between air holes was around 254 nm, and average air-holes separation was 3.96 μm. In the case of five spiral arms, we maintain good confinement by increasing air-hole radius in contrast to other designs that use more arms [34]. The spatial profile of the fundamental mode for five spiral arms, shown as an inset of Fig. 3(a),

exhibits excellent field confinement inside the central core region, enabling stronger nonlinear interaction compared to traditional microstructured fibers.

Before simulating SC generation, it is important to consider the damage threshold of ChG materials. GeAsSe-based glass has the lowest damage threshold at an average power density of 30 kW/cm^2. The damage threshold increases significantly when selenium-based glass is progressively replaced with the sulphide-based glass [27]. Even then, the ChG fiber core could be damaged if the peak intensity of pump pulses reaches 30 GW/cm^2, or the average power density at the input facet of the fiber exceeds 100 kW/cm^2. Paying attention to these factors, we designed our GeAsSe microstructured fibers for MIR SC generation such that the required peak power of pump pulses is at most 3 kW. For SC simulations, we utilize the GVD curves shown in Figures 2(a), 2(b), and 3(a) for the three optimized fiber structures. The linear propagation loss (α) at a pump wavelength of 3.1 μm is taken to be 0.5 dB/cm. The value of nonlinear refractive index used in our numerical simulations was reduced by a factor of two from its known value of $n_2 = 5.2 \times 10^{-18}$ m^2/W at 1.55 μm [19]. The effective mode area was calculated numerically and is different for different fibers: A_{eff} = 7.06 [red curve in Fig. 2(a)] and 9.41 μm^2 [black-curve in Fig. 2(a)], resulting in a nonlinear coefficient of γ = 1.24 and 0.93 W^{-1}/m and $D \approx$ 44 and 20 ps/nm/km, respectively, at the pump wavelength of 3.1 μm. Similarly, A_{eff} was 6.83 [red curve in Fig. 2(b)] and 9.36 μm^2 [black-curve in Fig. 2(b)], yielding γ = 1.28 and 0.93 W^{-1}/m and $D \approx$ 41 and 12 ps/nm/km, respectively. The effective mode areas for the ES-PCF were A_{eff} = 6.12 [red curve in Fig. 3(a)] and 8.94 μm^2 [black-curve in Fig. 3(a)] resulting γ = 1.42 and 0.98 W^{-1}/m and $D \approx$ 50 and 17 ps/nm/km, respectively, at the pump wavelength of 3.1 μm. For all cases, we have performed SC simulations using A_{eff} obtained at our pump wavelength numerically. Inclusion of the wavelength dependence of A_{eff} may change our results quantitatively but the qualitative behaviour is expected to remain the same.

4. SUPERCONTINUUM GENERATION FOR THREE FIBER DESIGNS

We first consider a triangular-core fiber for SC generation. We calculate higher-order dispersion terms up to 10$^{\text{th}}$ order at the pump wavelength of 3.1 μm using the solid red GVD curve in Fig. 2(a) for the triangular core base and perform numerical simulations using Eq. (4) for peak power levels between 0.2 and 3 kW; the results are shown in Fig. 4(a). As expected, the spectrum extends farther into the long-wavelength region with increasing pump power. Figure 4(b) compares the SC spectra for the two GVD curves in Fig. 2(a) at the largest peak power of 3 kW. The fiber with the dotted black GVD curve performs better and produces a broader SC extending up to 7.5 μm at a level of -30 dB from the peak. However, we have found that it is not possible to extend the SC further into the MIR region using a triangular-core fiber, if we limit the largest peak power to 3 kW.

We next consider the hexagonal PCF. Evaluating higher-order dispersion terms up to 10$^{\text{th}}$ order using the GVD curves shown in Fig. 2(b), we have carried out numerical simulations for the same power levels in the range of 0.2 to 3 kW, and the results are shown in Fig. 5(a). Once again, the spectrum extends farther into the long-wavelength region with increasing pump power. Figure 4(b) compares the SC spectra for the two GVD curves in Fig. 2(b) at the largest peak power of 3 kW. The fiber with

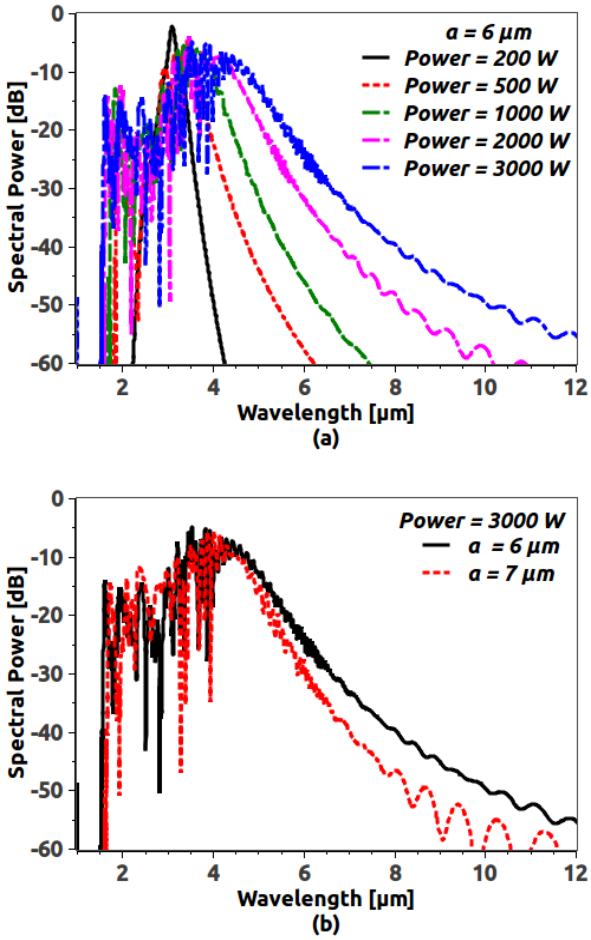

Fig. 4. Output spectra for a TC fiber: (a) using the solid red GVD curve shown in Fig. 2(a) for peak powers between 200 and 3000 W; (b) using the two GVD curves in Fig. 2(b) with 3000 W peak power pulses.

the solid red GVD curve performs better this time and produces a broader SC extending up to 8 μm at a level of -30 dB from the peak. This is somewhat surprising since GVD is larger for the red curve. The reason is related to the lower effective mode area for this fiber that helps to enhance the strength of various nonlinear effects responsible for the SC generation.

Finally we focus on the ES-PCF's performance for SC generation. Using the GVD curve shown by a red-line in Fig. 3(a) and a sech pulse of 85-fs duration (FWHM) for numerical simulation, we obtained the SC spectra shown in Fig. 6(a) when the peak power of pump pulses was varied between 0.2 and 3 kW. A comparison with Figs. 4(a) and 5(a) obtained under the same operating conditions for the other two fiber geometries shows clearly the advantages of using the ES-PCF geometry. The spectrum obtained for pulses with 3-kW peak power extends beyond 11 μm and is more than three octaves wide for the red GVD curve shown in Fig. 3(a). However, it is important to optimize the fiber design. Figure 6(b) shows how much the spectrum changes if one uses the GVD curve shown by the black line in Fig. 3(a). The new design has six spiral arms instead of five and the air-hole radius is reduced from 1.32 to 0.92 μm. Clearly, the fiber with five arms performs much better if the goal is to extend SC bandwidth beyond 11 μm. The important point to empha-

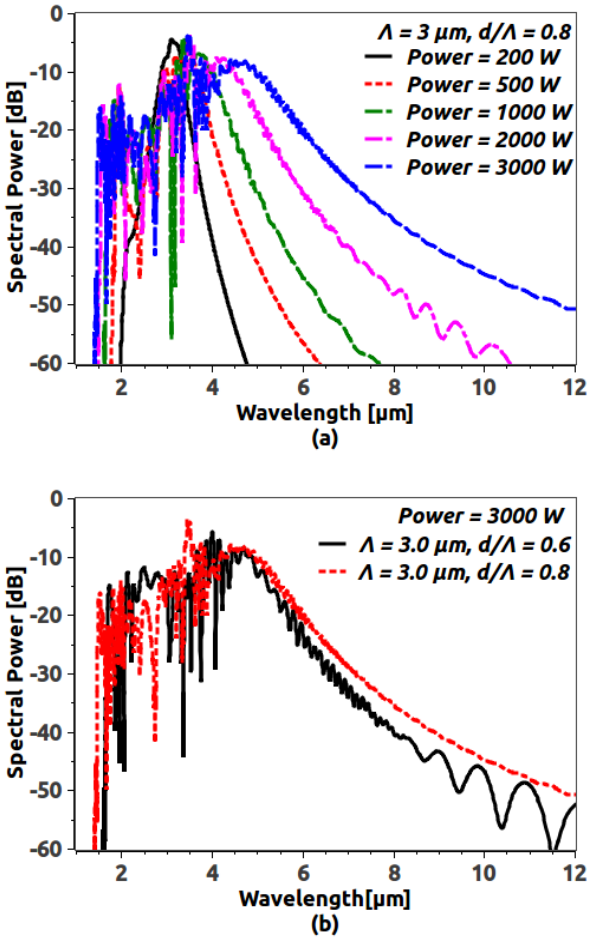

Fig. 5. Output spectra for hexagonal PCF: (a) using the solid red GVD curve in Fig. 2(b) for peak powers between 200 and 3000 W; (b) using the two GVD curves in Fig. 2(b) with 3000 W peak power pulses.

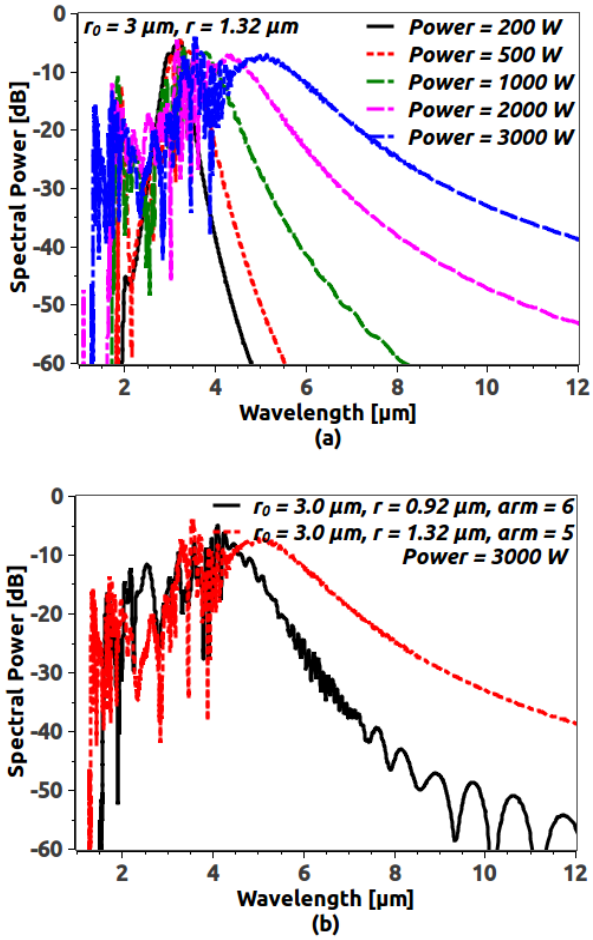

Fig. 6. Output SC spectra for ES-PCF: (a) using the solid red GVD curve in Fig. 3(a) for peak powers between 200 and 3000 W; (b) using the two GVD curves in Fig. 3(a) with 3000 W peak power pulses.

size is that the ES-PCF geometry is superior to other geometries because it allows much more control over the dispersive properties of the fiber by varying the four design parameters. Our results show that increasing the number of arms does not help and is even counterproductive. The use of five arms also allow us to increase the air-hole radius to near to 1.3 μm, which helps to keep the separation between air holes above the fabrication tolerance.

The spectra shown in Figs. 4-6 do not reveal how the SC evolves inside the fiber. The first two columns in Fig. 7 compare the temporal and spectra evolutions of pump pulses along the 1-cm length of the three fibers with different hole geometries corresponding to the three output spectra shown by the red curves in Figs 4-6. The dispersion lengths of the 85-fs pump pulse in three fibers are L_D = 10.2, 11.1, and 9.1 mm (top to bottom in Fig. 7) and the corresponding nonlinear lengths at a peak power of 3 kW are L_{NL} = 0.27, 0.26, and 0.23 mm. These values correspond to soliton orders $N = \sqrt{L_D/L_{NL}}$ of about 6, 7, and 6 for the three cases (top to bottom in Fig. 7). In all three cases, SC formation is mainly dominated by the soliton fission process occurring at a distance of 1.7 mm (top and middle) and 1.5 mm (bottom). The temporal and spectra evolutions exhibit qualitatively similar features in all three cases, namely multiple fundamental solitons are produced after the fission, whose spectra shift toward the long-wavelength side owing to intrapulse Raman scattering, producing multiple spectral peaks in the spectra seen in Fig. 7 (middle column). One can also see that a dispersive wave is generated at a wavelength near the first ZDWs of the fibers lying in the normal-dispersion regime of our proposed three designs. In spite of these similarities, slightly earlier fission of the sixth-order soliton in the case of the ES-PCF (bottom) leads to a much wider SC that extends over more than three octaves and covers a wavelength range from 1.3 to 11 μm. The spectral and temporal differences in the three cases are also apparent in the spectrograms shown in the third column of Fig. 7.

Figure 8 compares the output spectra for the three different microstructured fibers for each pair of GVD curves shown in this paper. The SC spectra obtained here do not exhibit flatness that is often desired for practical applications. It may be possible to improve SC flatness by optimizing further the dispersive properties of the fiber. However, due to a high index contrast across the core-cladding interface, the effective mode index of ChG microstructured fibers varies rapidly, which in turn results in larger values of the third-order dispersion parameter (β_3), especially near the zero-dispersion wavelengths. Such large

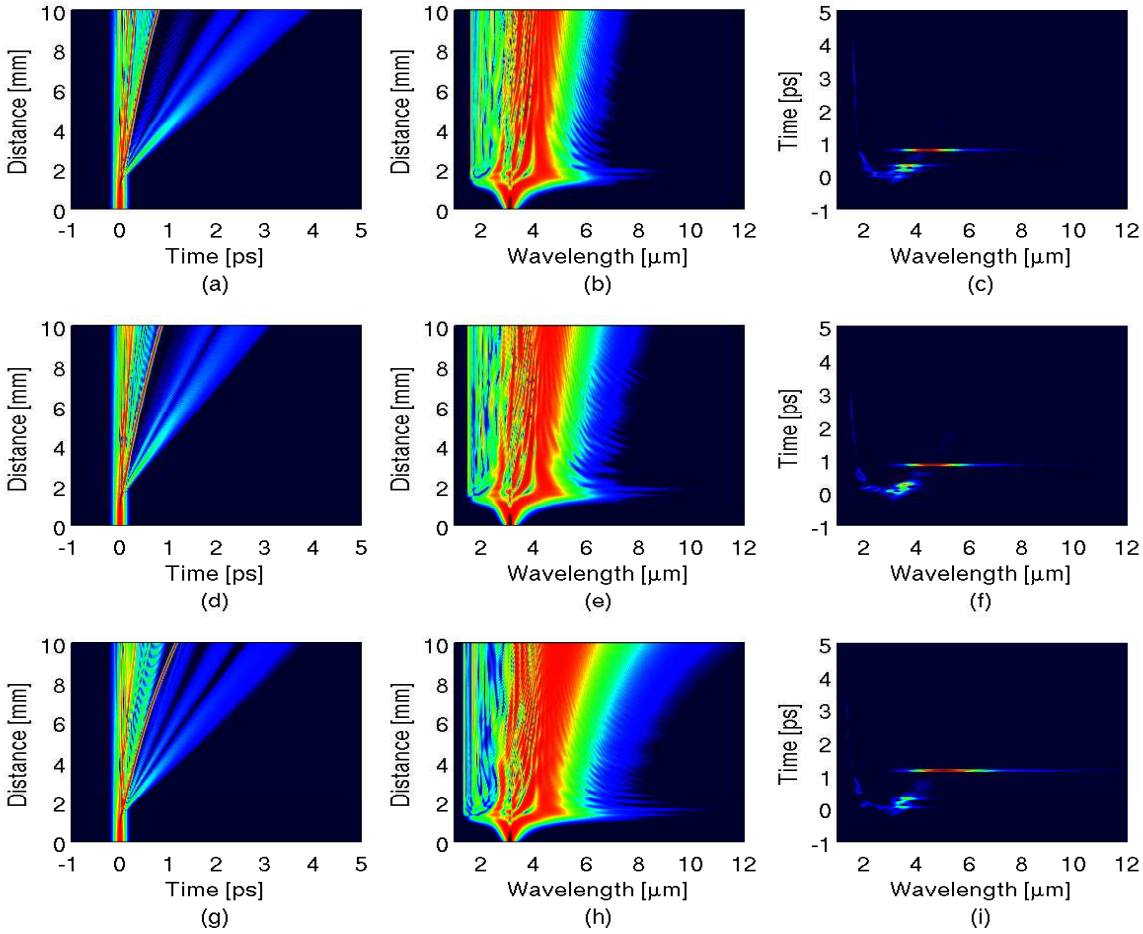

Fig. 7. Temporal evolution (left column), Spectral evolution (middle column), and Spectrogram (right column) at the fiber output for three fibers with different hole geometries. Top, middle, and bottom rows correspond to the output spectra shown by the red curve in Figs. 4 to 6, respectively.

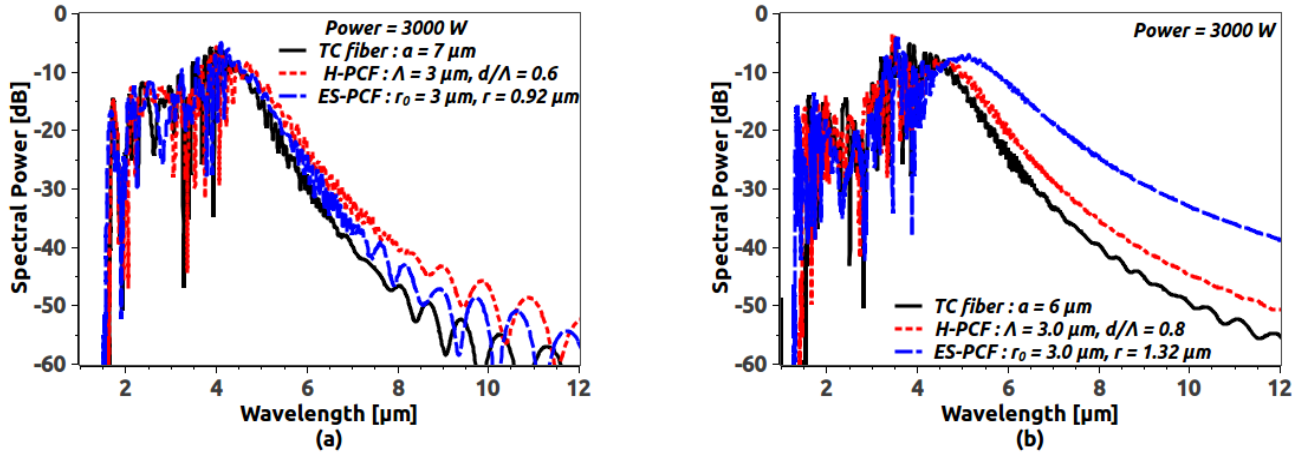

Fig. 8. Comparison SC spectra for three different ChG microstructured fibers: (a) for higher effective mode area GVD curves (black lines) in Figs. 2(a), 2(b), and 3(a); (b) for lower mode effective area GVD curves (red lines) in Figs. 2(a), 2(b), and 3(a). In all cases, pump pulses at 3.1 μm have 3 kW peak power.

values make it difficult to realize a relatively flat SC. Figure 8(a) shows the SC spectra for higher effective mode area designs with smaller GVD values and Fig. 8(b) shows the SC spectra for fibers with smaller mode areas and comparatively higher GVD values. We see that the spectra are quite close to each other for all three fiber designs in Fig. 7(a). However, much larger difference occur in the case of Fig. 7(b). These result suggest that both a smaller effective mode area and a flatter dispersion profile are critical for producing ultra-broadband SC extending to wavelengths beyond 11 μm.

5. CONCLUSIONS

In this paper, we have demonstrated numerically that the use of dispersion-engineered ChG microstructured fibers should allow one to generate an ultra-broadband SC in the MIR region that extends beyond 11 μm. We considered three fiber geometries based on $Ge_{11.5}As_{24}Se_{64.5}$ glass and optimized the dispersive properties of resulting fibers by varying the design parameters associated with each geometry. We found that the ES-PCF geometry is superior to other two geometries because it provides more control over fiber's dispersive properties. Microstructured fiber based on this geometry can be easily fabricated from soft glasses by the extrusion technique [32], or even by the stacking technique [33]. Using pump pulses at a wavelength of 3.1 μm with a relatively low peak power of 3 kW, we obtained a SC spectrum covering a wavelength range from 1.3 μm to beyond 11 μm ($>$ 3 octaves). To the best of our knowledge, this is the broadest MIR SC simulated at a relatively low peak power of 3 kW using a GeAsSe-based chalcogenide microstructured fiber. The ES-PCF design resulted in a lower mode effective area (which increases the nonlinear parameter) and shows flatter dispersion than the other two geometries we studied. The key feature of the ES-PCF based design is that the cladding containing air holes is made of the same material as the core. As a result, the ChG microstructured fibers do not suffer from cladding absorption that has limited the performance of ChG planar waveguides and ChG step-index fibers. By increasing the pump power or/and by shifting the pump wavelength to beyond 4 μm while adjusting the ES-PCF design parameters suitably, it should be possible to extend the SC to beyond 14 μm with our proposed $Ge_{11.5}As_{24}Se_{64.5}$ ES-PCF.

REFERENCES

1. J. Hu, C. R. Menyuk, L. B. Shaw, J. S. Sanghera, and I. D. Aggarwal, "Maximizing the bandwidth of supercontinuum generation in As_2Se_3 chalcogenide fibers," Opt. Exp. **18**(3), pp. 6722–6739 (2010).
2. J. M. Dudley and J. R. Taylor, "Ten years of nonlinear optics in photonic crystal fiber," Nat. Photonics **3**, pp. 85–90 (2009).
3. B. J. Eggleton, B. Luther-Davies, and K. Richardson, "Chalcogenide photonics," Nat. Photonics **5**, pp. 141–148 (2011).
4. I. D. Aggarwal and J. S. Sanghera, "Development and applications of chalcogenide glass optical fibers at NRL," J. Optoelectron. Adv. Mater. **4**(3), pp. 665–678 (2002).
5. J. M. Dudley, G. Genty, and S. Coen, "Supercontinuum generation in photonic crystal fiber," Rev. Mod. Phys. **78**, pp. 1135–1184 (2006).
6. G. Chang, T. B. Norris, and H. G. Winful, "Optimization of supercontinuum generation in photonic crystal fibers for pulse compression," Opt. Lett. **28**, pp. 546–548 (2003).
7. K. M. Hilligsoe, T. V. Andersen, H. N. Paulsen, C. K. Nielsen, K. Molmer, S. Keiding, R. Kristiansen, K. P. Hansen, and J. J. Larsen, "Supercontinuum generation in a photonic crystal fiber with two zero dispersion wavelengths," Opt. Exp. **12**, pp. 1045–1054 (2004).
8. W. J. Wadsworth, N. Joly, J. C. Knight, T. A. Birks, F. Biancalana, and P. St. J. Russell, "Supercontinuum and four-wave mixing with Q-switched pulses in endlessly single-mode photonic crystal fiber," Opt. Exp. **12**, pp. 299–308 (2004).
9. W. J. Wadsworth, A. Ortigosa-Blanch, J. C. Knight, T. A. Birks, T. P. M. Man, and P. St. J. Russell, "Supercontinuum generation in photonic crystal fibers and optical fiber tapers: a novel light source," J. Opt. Soc. Am. B **19**, pp. 2148–2155 (2002).
10. P. Falk, M. H. Frosz, and O. Bang, "Supercontinuum generation in a photonic crystal fiber with two zero-dispersion wavelengths tapered to normal dispersion at all wavelengths," Opt. Exp. **13**(19), pp. 7535–7540 (2005).
11. C. Wei, X. Zhu, R. A. Norwood, F. Seng, and N. Peyghambarian, "Numerical investigation on high power mid-infrared supercontinuum fiber lasers pumped at 3 μm," Opt. Exp. **21**(24), pp. 29488–29504 (2013).
12. X. Gai, T. Han, A. Prasad, S. Madden, D. Y. Choi, R. Wang, D. Bulla, and B. Luther-Davies, "Progress in optical waveguides fabricated from chalcogenide glasses," Opt. Exp. **18**(25), pp. 26635–26646 (2010).
13. M. R. Karim, B. M. A. Rahman, and G. P. Agrawal, "Dispersion engineered $Ge_{11.5}As_{24}Se_{64.5}$ nanowire for supercontinuum generation: A parametric study," Opt. Exp. **22**(25), pp. 31029–31040 (2014).
14. P. Ma, D. Y. Choi, Y. Yu, X. Gai, Z. Yang, S. Debbarma, S. Madden, and B. Luther-Davies, "Low-loss chalcogenide waveguides for chemical sensing in the mid-infrared," Opt. Exp. **21**(24), pp. 29927–29937 (2013).
15. L. B. Shaw, R. R. Gattass, J. S. Sanghera, and I. D. Aggarwal, "All-fiber mid-IR supercontinuum source from 1.5 to 5 μm," Proc. SPIE **7914** (79140P), pp. 1–5 (2011).
16. J. Fatome, C. Fortier, T. N. Nguyen, T. Chartier, F. Smektala, K. Messaad, B. Kibler, S. Pitois, G. Gadret, C. Finot, J. Troles, F. Desevedavy, P. Houizot, G. Renversez, L. Brilland, and N. Traynor, "Linear and nonlinear characterizations of chalcogenide photonic crystal fibers," J. Lightwave Technol. **27**(11), pp. 1707–1715 (2009).
17. X. Gai, D. Choi, S. Madden, Z. Yang, R. Wang, and B. Luther-Devies, "Supercontinuum generation in the mid-infrared from a dispersion-engineered As_2S_3 glass rib waveguide," Opt. Lett. **37**(18), pp. 3870–3872 (2012).
18. Y. Yu, X. Gai, T. Wang, P. Ma, R. Wang, Z. Yang, D. Choi, S. Madden, and B. Luther-Davies, "Mid-infrared supercontinuum generation in chalcogenides," Opt. Mater. Exp. **3**(8), pp. 1075–1086 (2013).
19. Y. Yu, B. Zhang, X. Gai, P. Ma, D. Choi, Z. Yang, R. Wang, S. Debbarma, S. J. Madden, and B. Luther-Davies, "A broadband, quasi-continuous, mid-infrared supercontinuum generated in a chalcogenide glass waveguide," Laser Photonics Rev. pp. 1–7 (2014).
20. M. R. Karim, B. M. A. Rahman, and G. P. Agrawal, "Mid-infrared supercontinuum generation using dispersion-engineered $Ge_{11.5}As_{24}Se_{64.5}$ chalcogenide channel waveguide," Opt. Exp. **23**(5), pp. 6903–6914 (2015).
21. H. Liang, P. Krogen, R. Grynko, O. Novak, C. L. Chang, G.J. Stein, D. Weerawarne, B. Shim, F.X. Kärtner, and K. H. Hong, "Three-octave-spanning supercontinuum generation and sub-two-cycle self-compression of mid-infrared filaments in dielectrics," Opt. Lett. **40**, 1069-1072 (2015).
22. A. B. Salem, R. Cherif, and M. Zghal, "Tapered As2S3 chalcogenide photonic crystal fiber for broadband mid-infrared supercontinuum generation," Frontiers in Optics 2011/Laser Science XXVII OSA Technical Digest (Optical Society of America, 2011), paper FMG6, doi:10.1364/FIO.2011.FMG6.
23. I. Kubat, C.R. Petersen, U.V. Mϕller, A. Seddon, T. Benson, L. Brilland, D. Mechin, P.M. Moselund, and O. Bang, "Thulium pumped mid-infrared 0.9-9 μm supercontinuum generation in concatenated fluoride and chalcogenide glass fibers," Opt. Exp. **22**, 3959-3967 (2014).
24. D. D. Hudson, M. Baudisch, D. Werdehausen, B. J. Eggleton, and J. Biegert, "1.9 octave supercontinuum generation in a As_2S_3 step-index fiber driven by mid-IR OPCPA," Opt. Lett. **39**(19), pp. 5752–5755 (2014).
25. C. R. Petersen, U. Mϕller, I. Kubat, B. Zhou, S. Dupont, J. Ramsay, T. Benson, S. Sujecki, M. Abdel-Moneim, Z. Tang, D. Furniss, A. Seddon, and O. Bang, "Mid-infrared supercontinuum covering the 1.4-13.3

μm molecular fingerprint region using ultra-high NA chalcogenide step-index fiber," Nat. Photonics **8**, pp. 830–834 (2014).
26. U. Mϕller, Y. Yu, I. Kubat, C. R. Petersen, X. Gai, L. Brilland, D. Mechin, C. Caillaud, J. Troles, B. Luther-Davies, and O. Bang, "Multi-milliwatt mid-infrared supercontinuum generation in a suspended core chalcogenide fiber," Opt. Exp. **23**(3), pp. 3282–3291 (2015).
27. Y. Yu, X. Gai, C. Zhai, S. Qi, W. Guo, Z. Yang, R. Wang, D. Choi, S. Madden, and B. Luther-Davies, "1.8-10 μm mid-infrared supercontinuum generation in a step-index chalcogenide fiber using low peak pump power," Opt. Lett. **40**(6), pp. 1081–1084 (2015).
28. R. J. Weiblen, A. Docherty, J. Hu, and C. R. Menyuk, "Calculation of the expected bandwidth for a mid-infrared supercontinuum source based on As_2S_3 chalcogenide photonic crystal fibers," Opt. Exp. **18**(25), pp. 26666–26674 (2010).
29. K. J. Blow and D. Wood, "Theoretical description of transient stimulated Raman scattering in optical fibers" IEEE J. Quantum Electron. **25**(12), pp. 2665–2673 (1989).
30. B. M. A. Rahman and J. B. Davies, "Finite-element solution of integrated optical waveguides," J. Lightwave Technol. **2**, pp. 682–688 (1984).
31. F. Silva, D. R. Austin, A. Thai, M. Baudisch, M. Hemmer, D. Faccio, A. Couairon, and J. Biegert, "Multi-octave supercontinuum generation from mid-infrared filamentation in a bulk crystal," Nat. Commun. **3**(807), pp. 1–5 (2012).
32. A. Agrawal, N. Kejalakshmy, B. M. A. Rahman, and K. T. V. Grattan, "Soft glass equiangular spiral photonic crystal fiber for supercontinuum generation," IEEE Photonics Technol. Lett. **21**(22), pp. 1722–1724 (2009).
33. A. Agrawal, Y. O. Azabi, and B. M. A. Rahman, "Staking the equianguar spiral," IEEE Photonics Technol. Lett. **25**(3), pp. 291–294 (2013).
34. A. Agrawal, M. Tiwari, Y. O. Azabi, V. Janyani, B. M. A. Rahman, and K. T. V. Grattan, "Ultrabroad supercontinuum generation in a tellurite equiangular spiral photonic crystal fiber," J. of Modern Opt. **60**(12), pp. 956–962 (2013).